Correction of Coherent Interference in Wave-Resolving Nearshore Models and Validation with Experimental Data

Simon Treillou, Patrick Marchesiello, Christine M. Baker

▶ **To cite this version:**

Simon Treillou, Patrick Marchesiello, Christine M. Baker. Correction of Coherent Interference in Wave-Resolving Nearshore Models and Validation with Experimental Data. 2024. ird-04511517

HAL Id: ird-04511517
https://ird.hal.science/ird-04511517

Preprint submitted on 22 Apr 2024

HAL is a multi-disciplinary open access archive for the deposit and dissemination of scientific research documents, whether they are published or not. The documents may come from teaching and research institutions in France or abroad, or from public or private research centers.

L'archive ouverte pluridisciplinaire **HAL**, est destinée au dépôt et à la diffusion de documents scientifiques de niveau recherche, publiés ou non, émanant des établissements d'enseignement et de recherche français ou étrangers, des laboratoires publics ou privés.

Correction of coherent interference in wave-resolving nearshore models and validation with experimental data

Simon Treillou[a,*], Patrick Marchesiello[a], Christine M. Baker[b]

[a] *Université de Toulouse, LEGOS (IRD/CNES/CNRS/UT3), Toulouse, France*
[b] *Department of Civil & Environmental Engineering, Stanford University, Stanford, CA, USA*

Abstract

Here we address the problem of coherent interference that arises in double-sum wavemakers of wave-resolving models. Identified as a key problem for experimental and numerical simulations since the late 1970s, this problem induces spurious persistent longshore variability and affects nearshore dynamics. To overcome this problem, we present the implementation of a single-sum wavemaker in the 3D wave-resolving model CROCO. The new wavemaker, which assigns only one pair of direction and frequency values to each component of the wave spectrum, definitively prevents coherent interference, unlike a conventional double-sum wavemaker that allows waves of different direction to share the same frequency. Each wave component must also strictly comply with the periodicity rules, to avoid any spurious boundary dynamics. We validate the single-sum wavemaker with experimental data collected in a wave basin with longshore-uniform bathymetry and compare results with the double-sum wavemaker simulations. We show that the new wavemaker produces transient rips devoid of any coherent interference effect and that, consequently, the model statistics closely match the experimental data. The new wavemaker therefore guarantees statistical integrity while reducing computational costs, a necessary step for realistic wave-resolving studies of nearshore dynamics.

Keywords: Coherent interference, Wave-resolving model, Wavemaker, Wave basin, Directional spread

*Corresponding author
Email address: simon.treillou@ird.fr (Simon Treillou)

1. Introduction

The nearshore region, consisting of the surf zone (from shoreline to breaking point) and the inner shelf (up to approximately 20 meter depth), is a turbulent area, with various time and space scales interacting and coexisting with each other. Understanding the processes that govern transport and circulation in this region is of critical importance for many reasons: health issues associated with coastal pollutants (Boehm et al., 2005), safety of users exposed to drowning due to rip currents (Woodward et al., 2013), ecosystem issues associated with coastal retention or dispersal of plankton or larvae (Moulton et al., 2023; Shanks et al., 2017), and sediment transport and morphological changes (Marchesiello et al., 2022).

One of the most important processes for cross-shore exchange between the surf and shelf are rip currents. They are narrow offshore directed flow of time scale from $\mathcal{O}$(1 min) to much longer $\mathcal{O}$(1 hr) and cross-shore spatial scale $\mathcal{O}$(100 m). Rip currents are particularly important for cross-shore exchanges between the beach and the continental shelf, as they can extend seaward over a width 2 to 3 times that of the surfzone (Kumar and Feddersen, 2017). Recent studies also underline the importance of rip currents in the shelf circulation of $\mathcal{O}$(1 km) (Wu et al., 2021). Rip currents are referred to as channeled (bathymetric) rip currents when driven by longshore variability in the bathymetry (Castelle, 2016), or transient rip currents (flash rips) when resulting from discontinuous breaking due to short crested waves (Peregrine, 1998; Clark et al., 2012; Johnson and Pattiaratchi, 2004). While channeled rip currents are relatively well understood (e.g., Marchesiello et al. 2015), flash rips are a more recent topic and are still incompletely assessed, even though they are thought to represent a large part of nearshore activity (Tang and Dalrymple, 1989).

The simulation of transient rip currents requires wave-resolving (or phase-resolving) models, which have the unambiguous ability to represent short-crested waves and associated vorticity injection into the surfzone. A necessary step in wave-resolving simulation is finding a way to force the wave field at the offshore boundary. There are three main options to do this: a wave generator at a source point inside the domain (Wei et al., 1999); a wave generator at a fixed offshore boundary point (Marchesiello et al., 2021); or a moving boundary simulating a

pad (Higuera et al., 2015), but this technique is only used to generate long waves. CROCO, the Coastal and Regional Ocean Community model used in the present study, focuses on the second method. More importantly here, regardless of the wave imposition technique, most wave-resolving models use double summation to represent a wave spectrum that distributes wave energy as a function of frequency and direction.

Double-sum wavemakers have been used extensively and helped improve our understanding of nearshore dynamics (Hally-Rosendahl et al., 2014; Suanda and Feddersen, 2015; Spydell et al., 2019). However, they suffer from a phase-locking or coherent interference phenomenon. This can be understood by considering two wave trains propagating towards the beach from different directions. These waves interfere, generating a longshore modulation of their amplitude (short-crested waves) which migrates along the beach at a speed increasing with their frequency difference (Fowler and Dalrymple, 1990). For waves of same frequency, the migration speed is zero, leaving a permanent pattern of short-crested waves (coherent interference) that always break at the same point on the beach, generating persistent rip currents in deterministic locations via more similar mechanisms to bathymetrically-driven rip currents. Coherent interference from intersecting ocean wave trains can be found in nature, e.g., resulting from reflection on a breakwater (Dalrymple, 1975; Smit and Janssen, 2013; Zhang et al., 2022). However, they tend to arise in models for nonphysical reasons, simply because of the deterministic nature of discretized wave generators. This can affect the model results in ways that are not necessarily noticed by modelers, as spurious rip currents are mixed among other rip current events.

This problem was reported long ago (Jefferys, 1987; Miles and Funke, 1989), noting the paradox of simulating a random sea state with a deterministic wavemaker. Early recommendations were to use stochastic implementations, but these models require a lot of computing time to be statistically reliable. Deterministic wavemakers therefore offer advantages, provided that wave coherence and associated stationary interference can be dealt with. A common solution is to increase the number of frequencies in the wavemaker spectrum, but this only reduces the probability of coherent interference, and is also computationally expensive. Building on previous work (Pascal and Bryden, 2011; Salatin et al., 2021), here

we implement a single-sum wavemaker that is both computationally efficient and definitely devoid of coherent interference. To confirm that this is desirable in a numerical model, we validate the single-sum method and compare with the double-sum method for the first time with data from a directional wave basin experiment (Baker et al., 2023b). In addition, attention to energy conservation ensures that the wavemaker correction does not affect the integrity of the physical solution, and that it accurately represents reality. We hope that our work will increase the modeling community's awareness of the coherent interference problem, and offer a simple and computationally efficient solution to resolve it.

2. Methods

2.1. The 3D wave-resolving model CROCO

CROCO is a non-hydrostatic, free-surface, terrain-following model developed around the regional oceanic modeling system (Shchepetkin and McWilliams, 2005; Debreu et al., 2012). Its capabilities include high-performance computation of high-order discretized equations and coupling with atmospheric, wave, biogeochemical, sediment and turbulence models. It has been applied to a variety of configurations, from regional and shelf circulations to very fine-scale processes, such as wave-induced nearshore circulation (Marchesiello et al., 2015, 2021, 2022). In its non-hydrostatic version, CROCO is able to resolve individual wave propagation, shoaling and breaker-induced circulation. Breaking waves are treated as bores with a shock-capturing advection scheme (WENO5), which transfers steep wave energy to the mean currents, while part of the breaking wave energy is transferred to subgrid-scale turbulence via a k-ω turbulence closure model. The latter corrects for an overmixing problem posed in the potential (irrotational) flow region of non-breaking waves (Marchesiello and Treillou, 2023), allowing stratification to be correctly included in our studies. CROCO is therefore well suited to the study of 3D nearshore dynamics and surf-shelf exchange in a rotating, stratified framework. Nonetheless, the wavemaker corrections proposed in the present study are relevant for all wave-resolving models, including the classical Boussinesq type.

2.2. Default double-sum wavemaker

The double-sum wavemaker implemented in CROCO (Marchesiello et al., 2021) forces a spectrum of 3D linear waves at the offshore boundary, much like SWASH (Zijlema et al., 2011), while Funwave (Wei et al., 1999) typically uses similar forcing but with an interior source function[1]. In all cases, the frequency and directional distribution of wave energy is discretized via a double summation (Feddersen et al., 2011). The free surface and velocities at the offshore boundary are then, respectively, given by:

$$\eta_{bc}(y,t) = \sum_{i}^{N} a_i \sum_{j}^{M} d_j \cos(k_{y,i,j} y - \omega_i t - \phi_{i,j}) \tag{1}$$

$$u_{bc}(x,y,t) = \eta_{bc}(y,t)\omega_p \cos(\theta_m)\frac{\cosh(k_p(z+h))}{\sinh(k_p h)} \tag{2}$$

$$v_{bc}(x,y,t) = \eta_{bc}(y,t)\omega_p \sin(\theta_m)\frac{\cosh(k_p(z+h))}{\sinh(k_p h)} \tag{3}$$

where (x, y, z) are cross-shore, alongshore and vertical directions; a_i is the wave amplitude at each angular frequency ω_i from a given statistical distribution $S(\omega)$; d_j is the directional weight for wave angle θ_j from the given statistical distribution $D(\theta)$; $k_{y,i,j} = k_i \sin\theta_j$ is the alongshore wavenumber where k_i is the linear theory wavenumber: $\omega_i^2 = g\, k_i \tanh(k_i h)$ with h the water depth; θ_m is the mean wave angle; ω_p and k_p are peak frequency and wavenumber; $\phi_{i,j}$ is a uniformly distributed random phase; and N and M are respectively the number of frequencies and directions.

As described by Marchesiello et al. (2021), w_{bc} is here set to zero rather than the linear solution for w as only weak sensitivity to this choice was found. The depth-averaged (barotropic) velocities ($\bar{u}$,$\bar{v}$) are provided in the wavemaker because they are prognostic variables in our split-explicit model, advanced at the same time as the fast acoustic mode (see Marchesiello et al., 2021). The depth-averaged normal velocity $\bar{u}$ is supplemented at the

[1]FUNWAVE-TVD now has the option of a single-sum wavemaker following the study conducted by (Salatin et al., 2021)

boundary by an Eulerian anti-Stokes current, opposed to the Stokes drift and thus closing the mass balance. We do not directly impose the depth-averaged value of u_{bc} but the value of the incoming characteristic of the shallow water system as in Flather-type conditions (Marchesiello et al., 2001; Blayo and Debreu, 2005):

$$\bar{u} = \bar{u}_{bc} - \sqrt{\frac{g}{h}}(\eta - \eta_{bc}) \tag{4}$$

This allows infragravity waves generated inside the domain to propagate out as long waves, while ensuring a near conservation of mass and energy through the open boundary. Likewise, the baroclinic components (u_{bc},v_{bc},w_{bc}) are applied via an adaptive radiation condition which helps short waves and 3D flow perturbations to leave the domain with only a small effect on the interior solution (Marchesiello et al., 2001).

In this study, the spectrum distributions is the product of a JONSWAP frequency spectrum $S(\omega)$ (Goda, 2000) and a Gaussian-type directional spectrum $D(\theta)$ (Feddersen et al., 2011): $S(\omega, \theta) = S(\omega) \times D(\theta)$. The JONSWAP spectrum is formulated as follows:

$$S(\omega) = H_s^2 \beta_J \omega_p^4 \omega^{-5} \exp[-1.25\omega^{-4}\omega_p^4]\gamma^r \tag{5}$$

H_s is the significant wave height, ω_p, the peak wave frequency, and γ^r, the peak enhancement factor, with:

$$r = \exp\left[-\frac{1}{2}\left(\frac{\omega - \omega_p}{\sigma_\omega \omega_p}\right)^2\right] \tag{6}$$

$$\sigma_\omega = \begin{cases} 0.07, & \text{if } \omega \leq \omega_p \\ 0.09, & \text{if } \omega > \omega_p \end{cases} \tag{7}$$

$$\beta_J = \frac{0.06238(1.094 - 0.01915\log\gamma)}{0.23 + 0.0336\gamma - 0.185(1.9 + \gamma)^{-1}} \tag{8}$$

The directional spectrum around the mean direction θ_m, with directional spread σ_θ, is:

$$D(\theta) = \exp\left[-\left(\frac{\theta - \theta_m}{1.5\sigma_\theta}\right)^2\right] \tag{9}$$

with $\int_{\theta_{min}}^{\theta_{max}} D(\theta)d\theta = 1$ to ensure that the directional spread (σ_θ) around the mean wave angle does not affect wave energy.

2.3. Coherent interference principle

We illustrate here the principle behind coherent interference by reproducing the solution given by Fowler and Dalrymple (1990) for two wave trains propagating towards the beach with different wavenumbers and frequencies. For simplicity (and without modifying the general idea), we consider waves of same amplitude a propagating at an angle θ around the x axis normal to the coast (θ is the directional spread in this case and $\theta_m = 0$). The mean wavenumber k is along the x axis, while the difference between the wavenumbers $\Delta k = 2k \sin\theta \sim 2k\theta$ lies along the y longshore axis. Similarly, we consider that the mean frequency is ω and the frequency difference between the two wave trains is $\Delta\omega$. In this case, the wave interference solution for the free surface η is :

$$\eta(x, y, t) = 2a \sin(kx - \omega t) \cos[0.5(\Delta k\, y - \Delta\omega\, t)] \tag{10}$$

The total surface elevation consists of a carrier wave (k,ω) modulated by a time-dependent envelope propagating along the coast at speed $\Delta\omega/\Delta k$. The envelope produces short crested waves of length $\lambda_c = 2\pi/\Delta k = \pi/k\theta$ — as first suggested by Longuet-Higgins 1956 and shown to apply to the more general case by comparison with experimental data (Baker et al., 2023b). Longshore envelope migration occurs when $\Delta\omega \neq 0$, i.e. the envelope is phase-shifted. In this case, waves have no persistent longshore variations (illustrated with H_s in Fig. 1). However, if the wave trains share the same frequency ($\Delta\omega = 0$), the envelope phase is locked and the propagation speed is zero. In this case, H_s shows a pattern of nodes and antinodes along the beach (Fig. 1), i.e. short-crested waves constantly travel towards the same location on the beach, thus creating stationary rip currents as they break.

This phenomenon is at the root of the coherent interference problem of discrete double-sum wavemakers. In the real ocean, with a continuous frequency spectrum of random waves, the probability of phase-locking is minimal, over smooth topography at least, and generally only occurs in focal zones due to refraction, diffraction or reflection of monochromatic waves around obstacles such as breakwaters or headlands (Smit and Janssen, 2013). We will see that wave basin experiments also tend to show little coherent interference. We therefore consider the coherent interference generated by discretized double-sum wavemakers as spu-

rious, and seek a definitive solution to avoid it by preventing the generated wave trains from sharing the same frequency. This is made possible by simple summation, presented below.

2.4. Corrected single-sum wavemaker

In order to avoid coherent waves, i.e., waves of different directions having same frequencies, a solution is presented by Salatin et al. (2021). Double-sum is converted into a single-sum wavemaker where each wave component has specific frequency and direction. Single summation was proposed before with variations in the distribution of wave components (Jefferys, 1987; Miles and Funke, 1989; Pascal and Bryden, 2011), and a useful schematic view was given in Pascal (2012). Based on this previous work, we rewrite the free-surface wave boundary condition :

$$\eta_{bc}(y,t) = \sum_{i}^{N\times M} a_i \cos(k_{y,i} y - \omega_i t - \phi_i) \tag{11}$$

where a_i is now the amplitude of the i-th wave component taken as:

$$a_i = \sqrt{\frac{H_s^2\, \overline{D(\theta_i)}\, S(\omega_i) d\omega}{8 \sum_i S(\omega_i) d\omega}} \tag{12}$$

which is the product of the wave amplitude $A = \sqrt{H_s^2/8}$ with $H_s = 4\sqrt{\int S(\omega) d\omega}$, the square root of the normalized frequency spectrum $S(\omega)d\omega / \sum_i S(\omega_i)d\omega$ (with frequency resolution $d\omega$), and the square root of the normalized directional spectrum $\overline{D(\theta)}$:

$$\overline{D(\theta)} = \frac{D(\theta) \sum_i S(\omega_i) d\omega}{\sum_i D(\theta_i) S(\omega_i) d\omega} \tag{13}$$

The wave angles around the mean direction are:

$$\theta_i = (-1)^i \left(-\frac{\pi}{2} + \frac{\pi}{2} \frac{i-1}{N-1} \right) + \theta_m, \tag{14}$$

ensuring that all wave angles are included between $-\frac{\pi}{2}$ and $\frac{\pi}{2}$.

2.5. Periodic boundary conditions

Most nearshore circulation studies use periodic alongshore boundary conditions, to allow longshore drift to develop and surfzone eddies to propagate freely. It is therefore essential

that waves entering the domain satisfy these periodic conditions. Following the suggestion of Johnson and Pattiaratchi (2006), we impose that each i-th wave component satisfies the following equation:

$$k_{y,i} = k_i \sin\theta_i = \frac{2\pi p}{L_y} \tag{15}$$

where L_y is the domain longshore length and p an integer. This relationship guarantees that for each wave train component i (with given frequency and direction), there is an integer number of these waves projected in the longshore direction, as schematized in Fig. 2. This is sufficient to ensure periodicity. Otherwise, shadow zones can form, where strong wave height gradients can develop, generate parasite rip currents near the boundaries and affect longshore drift.

Periodization can be obtained by modifying the angle θ_i to satisfy Eq. 15 :

$$\theta_i = \arcsin\left(\frac{2\pi p}{k_i L_y}\right) \tag{16}$$

In CROCO, the directional spectrum and associated unrestricted wave angles are first calculated. Then, all wave angles are corrected according to Eq. 16, ensuring that the mean wave angle θ_m remains unchanged. The correction is made by selecting the integer p that produces the smallest change in θ_i (for the double-sum wavemaker, the correction is applied to all angles at each frequency). In practice, the differences between the original and corrected wave angles are relatively small and do not significantly impact the directional spectrum. All simulations presented in this article are therefore expected to respect boundary periodicity.

3. Validation with laboratory wave basin

3.1. Laboratory experiments

The data used to validate the new wavemaker comes from an experiment conducted in the Directional Wave Basin at the Oregon State University O.H. Hinsdale Wave Research Laboratory (Baker et al., 2023b). The goal of this experiment was to gain a better understanding of the processes involved in the generation of flash rips and surfzone eddies, by investigating the effect of directional spread on breaking crest length. For this purpose, a barred

Case	H_s (m)	T_p (s)	θ_m (°)	σ_θ (°)
G1a	0.28	2.1	-0.1	2.4
G1d	0.27	2.0	-3.3	26.1

Table 1: Significant wave height H_s, peak period T_p, mean wave angle θ_m and directional spread σ_θ for cases used in this study. H_s, T_p, θ_m and σ_θ were estimated at the offshore wave gauges and are used as wavemaker forcing conditions in the model.

beach was recreated in the wave basin, respecting the surf similarity number (ratio of wave steepness to slope) of real scale beaches. A 29-board piston-type wavemaker could simulate a continuous distribution of multidirectional waves with JONSWAP frequency spectrum of width $\gamma = 3.3$. Several experiments were run for a range of different significant wave heights, peak periods and directional spreads. These experiments are of high interest to validate our wavemaker as the wave basin is large enough (48.8 m long, 26.5 m wide) to investigate longshore variation of the wave field. Each run lasted 45 minutes ($\sim$ 1350 wave periods), providing sufficiently long time series to study coherent wave interference. The free surface and velocities were measured with in situ sensors (pressure gauges, ADVs, and resistance gauges). The in-situ sensors were deployed as longshore arrays: two offshore arrays, one on the inner shelf and two in the surfzone (Fig. 3). The in-situ sensors had a frequency of 100 Hz. We refer the reader to Baker et al. (2023b) for more details about the experiment.

We focus on two experiments with low (G1a) and high (G1d) directional spread and otherwise similar bulk wave statistics (Table 1). We use the wave conditions recorded onshore of the wavemaker rather than those theoretically imposed at the wavemaker, partly because directional errors affects the intended wave spectrum and do not, for example, allow G1a to be a truly unidirectional experiment (Baker et al., 2023b). We have verified that the two types of discretized wavemakers in the model give very similar results when directional spread is exactly zero (case G1a with σ_θ=0° gives H_s RMSE< 1mm), and that the differences in model results between the two wavemakers are due solely to directional spread.

Free surface model spectra ($S_{\eta\eta}$) are computed similarly to Baker et al. (2023b), using a Hanning window period of 256 s with an overlap period of 128 s and correcting for depth

	Single sum (50 freq.)	Double sum (50 freq.)	Double sum (300 freq.)	Random-phase (50 freq.)
$\langle\sigma_{\omega_z}\rangle_{SZ}$ (s^{-1})	0.03	0.16	0.08	0.03
$\langle\sigma_v\rangle_{SZ}$ $(m.s^{-1})$	0.01	0.05	0.02	0.01
$\langle\sigma_{H_s}\rangle$ (m)	0.02	0.04	0.03	0.02
H_s RMSE (m)	0.010	0.047	0.020	0.015

Table 2: Longshore standard deviation of 20-min time-averaged surface vertical vorticity (σ_{ω_z}), longshore velocity (v) and significant wave height (H_s) (see Fig. 5) for the model running case G1d with various wavemaker methods. RMSE between in-situ and simulations H_s for $t = 10 - 30$ min (see Fig. 6). σ_{ω_z} and σ_v are averaged in the surfzone ($27 < x < 31$ m) while σ_{H_s} is averaged on the whole domain. The RMSE of H_s indicating the error between model and data over the whole domain is also reported.

attenuation (frequency cutoff = 1.2 Hz) over a 20-minute time series (t =10-30 minutes, with 10 min of spin-up). The significant wave height (H_s) is calculated as $4\sqrt{\int_{0.3}^{1.2} S_{\eta\eta}(f)df}$. Velocity spectra are computed using a Hanning window period of 256 s with an overlap period of 128 s over the same 20-minute time series. Reducing the time series by half did not significantly affect the results.

3.2. Model configuration

The alongshore-uniform bathymetry in the model is identical to the experiment (Fig. 3), without smoothing. The position of the shoreline is time-dependent, owing to a wetting-drying scheme (Warner et al., 2013). The cross-shore and longshore domain lengths are respectively 20 m and 30 m. The horizontal resolution is $\Delta x = 0.1$ m and there are 10 vertical levels. The model time step is 0.003 s and total computed time is ∼30 min (∼900 wave periods were enough for significant results). The bottom stress is modeled as a quadratic friction using the law of the wall with roughness $z_{0,b} = 1 \times 10^{-5}$ m. Turbulent kinetic energy is solved via a $k - \omega$ turbulent closure model (Marchesiello and Treillou, 2023).

The wavemaker has a resolution of $N = 50$ frequencies (between 0.1 Hz and 2 Hz, i.e. between 0.2 and 2 times the peak frequency) and $M = 31$ directions, corresponding to default settings in FUNWAVE-TVD (Salatin et al., 2021). However, to be comparable with studies

using a larger number of frequencies, we have added an experiment with 300 frequencies for the double-sum wavemaker. This is 7% more expensive than the double-sum case with 50 frequencies, which is itself 20% more expensive than the single-sum wavemaker simulation (also with 50 frequencies). Unlike the laboratory experiment, the model's northern and southern boundaries are periodic, and the western (offshore) boundary is open to long waves. Wave-averaged and instantaneous fields are output every 12 s (corresponding to 6 peak periods) on the entire domain, while model results at specific grid points corresponding to the experimental stations are extracted at a frequency of $\sim$ 6 Hz.

3.3. Comparison of double and single sum wavemaker cases

Directional spreading produces short-crested waves, which can generate flash rips when they break in the surf zone. The G1d experiment, with its fairly large directional spread (σ_θ=26.1°), is particularly effective at generating surfzone eddies and flash rips, as illustrated by snapshots of vertical surface vorticity from the model solutions with double (50 freq.) or single-sum wavemakers (Fig. 4). In both cases, flash rips and smaller-scale rib structures, referred to as mini-rips (Marchesiello et al., 2021), can be observed in the surf zone. These rib structures with longshore scale of $\sim$1 m and frequencies in the infragravity band are associated with 3D shear instability of the undertow.

From the snapshots alone, the difference between the two simulations could be accounted for by the stochastic nature of the eddy field rather than coherent interference, but the 20-min time-averaged fields are unambiguous (Fig. 5 and Table 2). No stationary vorticity pattern is present in the case of the single-sum wavemaker, as might be expected if random waves were breaking on uniform longshore bathymetry (Fig. 5, left). Only a residual stochastic variability remains, due to the finite number of flash rip events during the experiment. However, in the case of the double-sum wavemaker, the time-averaged vorticity shows strong stationary rip currents, reminiscent of the patterns observed in the vorticity snapshot. In the case where 50 frequencies are used, the longshore standard deviation of time-averaged surfzone vorticity is 0.16 s^{-1} (see Table 2), whereas the single-sum wavemaker gives a lower value by an order of magnitude of 0.03 s^{-1}. With 300 frequencies, the double-sum wavemaker

is improved as it produces a lower longshore standard deviation of surfzone vorticity (0.08 s^{-1}), but it remains higher than that produced by the single-sum wavemaker, at a higher computational cost.

Stationary rip currents are also apparent on the longshore velocity field (Fig. 5, middle). With the double-sum wavemaker, the weak longshore drift expected from the mean wave angle ($\theta_m = -3.3°$) is hidden by a series of strong converging flows. These patterns are somewhat improved by the addition of wavemaker frequencies, but are much better corrected by the single-sum method, which produces a smooth mean longshore drift as expected. Note that the effect of double summation remains visible in case of weak directional spread (G1a, not shown), with coherent wave-induced stationary rips that remain prominent.

Finally, we compare the significant wave height fields in Figure 5 (right). Interestingly, the comparison between double and single wavemaker solutions has similar characteristics to the idealized case presented in Section 2.3 of two wave trains with or without frequency difference. The wave height band pattern in the double-sum wavemaker simulations, and the absence of this pattern in the single-sum wavemaker simulation, are reminiscent of the idealized solutions in Figure 1. In both idealized and realistic cases, the coherent interference associated with waves of different angles but same frequencies produces high and low H_s bands, correlating perfectly with the persistent rip currents appearing in the vorticity and velocity fields. The single-sum wavemaker, by avoiding interference from waves of the same frequency, presents a homogeneous H_s field.

3.4. Comparison with data

A comparison between double and single wavemakers has already been carried out (Salatin et al., 2021), but no direct comparison has been made with data, and it is not clear how realistic is the idea of eliminating all coherent interference in models. In particular, we wondered whether the uncertainty inherent in the forcing frequencies of the basin experiment was sufficient to preclude coherent interference. To answer this question, we present here a comparison between the model and the experimental data.

We showed in the last section that coherent interference patterns result in an alongshore-

varying H_s field, that manifest as elongated cross-shore bands of highs and lows. We therefore first assess whether these signs of coherent interference are present in the data by examining H_s longshore variability. Figure 6 shows H_s along the offshore gauges (at $x = 19$ m) in the G1d case, calculated from 20-minute time series. The experimental data show little longshore variability around the mean H_s value of 0.28 m, and present a good match with the single-sum wavemaker simulation. In contrast, the default double-sum wavemaker (with 50 frequencies) produces high longshore variability, with H_s as low as 0.19 m at some locations ($y = 9$ m), i.e. a third lower than the forcing value. The standard deviation of H_s reaches around 4 cm, compared with 2 cm for the single-sum wavemaker (in G1a, with low directional spread, the standard deviation is 0.8 cm and 0.04 cm for the double-sum and single-sum wavemakers, respectively). With 300 frequencies in G1d, the standard deviation reduces to 1.7 cm but coherent interference is still clearly present. The RMSE between the data and the single-sum wavemaker is around 1.0 cm, while it is around 4.7 cm for the 50-freq. double-sum wavemaker (with 2.0 cm with 300 freq.). It is important to note that, while laboratory experiments are prone to reflection and associated interference due to non-periodic boundaries, there is no evidence here of physical interference on the scale of that of the double-sum discretized wavemaker. The alongshore standard deviation of H_s in CROCO simulations are similar to FUNWAVE-TVD simulations with a single-sum wavemaker (Salatin et al., 2021; Nuss et al., in review).

The double-sum method not only affects longshore variability, but also the average wave energy in the domain. Figure 7 presents a cross-shore profile of H_s averaged in the longshore direction from all sensors. Here also, the single-sum wavemaker shows an excellent match with the data over the whole profile. For the double-sum wave maker, the coherent wave-induced H_s bands tend to cancel out when averaged alongshore, giving fairly similar cross-shore H_s profiles, but still leaving a negative bias of up to 2-3 cm (offshore stations), reduced by around half when the number of frequencies is increased to 300 (Fig. 5).

The effect of wavemaker types on nearshore dynamics can also be assessed using power spectra (Fig. 8 and 9). Model and data free surface spectra $S_{\eta\eta}$ at points offshore ($x = 19$m, $-9 < y < 9$m) and in the outer surf zone ($x = 28.4$m, $-8 < y < 3$m) are shown in Figure 8.

The longshore mean and standard deviation of $S_{\eta\eta}$ are closer to the data for the single-sum wavemaker at almost all frequencies. Specifically, the spurious longshore variability for the double-sum wavemaker is far too high (the double-sum wavemaker here is with 300 freq., and the variability is even greater with 50 freq.), particularly in the low-frequency range, but also in the swell band ($0.3 < f < 1.2$ Hz) (Salatin et al., 2021).

The S_{uu} cross-shore velocity spectra on the innershelf (Fig. 9) show similar differences to the free-surface spectra, with an even greater longshore standard deviation at low frequency for the double-sum wavemaker. Both wavemakers show a good match with the data in the longshore mean, and the difference lies mainly in the standard deviation. Consequently, the surfzone eddies are affected by persistent spurious rip currents, but the effect tends to cancel out over the domain.

4. Conclusion

Over the past decade, studies has been carried out to find a suitable way of forcing a random sea state into wave-resolving models. Here, we build on the work of Salatin et al. (2021) and others to define a wavemaker devoid of spurious coherent interference, apply it to the 3D wave-resolving model CROCO and validate it with experimental data. We show that a single-sum wavemaker that assigns only a pair direction and frequency values to each component of a wave spectrum definitively prevents coherent interference, in contrast to a conventional double-sum wavemaker that allows waves of different direction to share the same frequency. This method also saves a great deal of computing time — over 25% of the cost of the simulation, depending on the number of frequencies used in the first method to mitigate coherent interference. Another correction made to the wavemaker consists in periodizing each wave component by slightly modifying its direction. Similar correction is present in FUNWAVE-TVD (Salatin et al., 2021). The new wavemaker is then applied to a model setup of the laboratory wave basin experiment presented in Baker et al. (2023b).

In the double-sum wavemaker simulation, the generation of stationary rip currents from coherent interference is clearly visible in the mean vorticity field. The mean longshore drift also changes sign despite the longshore uniform bathymetry, and the significant wave

height shows bands of high and low values oriented in the shore-normal direction (creating longshore pressure gradients). Increasing the number of frequencies in the classical double-sum wavemaker reduces the observed biases, but they remain significant and affect the production of transient rip and surf zone eddies, as can be seen in the velocity power spectra. The single-sum wavemaker has none of these characteristics, and consistently reproduces the experimental data with regard to the magnitude and variation of surface elevation and velocities, therefore, likely more realistically representing the transient rip current behaviors.

While the classical double-sum method cannot compete with the single-sum method in terms of accuracy and cost, we have more successfully tested (see Table 2) the double-sum method of Johnson and Pattiaratchi (2006), which added a time-dependent random phase shift to mitigate the phase-locking effect (similar to the effect of random errors in the forcing frequencies of the laboratory experiment). Yet even in this case, the computational cost remains prohibitive compared with the single-sum method (in addition, the added random phase shift modifies, albeit slightly, the dispersion relation; Johnson and Pattiaratchi 2006).

On the basis of a validation which, for the first time, uses experimental data, we conclude that a single-sum wavemaker gives better results than the double-sum wavemaker at low computational cost. We expect that our study will increase confidence in future wave-resolving simulations, and provide a necessary step towards a more comprehensive investigation of rip currents, tracer dispersion or morphological evolution using this type of model.

CRediT authorship contribution statement

Simon Treillou: Conceptualization, Methodology, Software, Validation, Writing – original draft. **Patrick Marchesiello**: Methodology, Software, Validation, Supervision, Writing – review & editing. **Christine M. Baker**: Validation, Data Curation, Writing – review & editing.

Declaration of competing interest

The authors declare that they have no known competing financial interests or personal relationships that influenced the work reported in this paper.

Acknowledgement

This research has received support from a consortium of French research agencies, as part of CROCO's development project (Insu GdR n°2014 named CROCO) and from the French Naval Hydrographic and Oceanographic Service (SHOM DGA-Protevs II). Apart from these, all data were acquired by the authors and the CROCO source code is freely available at `www.croco-ocean.org`. The laboratory measurements are available at Design Safe (Baker et al., 2023a). Modeling data are available upon request.

References

Baker, C.M., Moulton, M., Palmsten, M., E., N., 2023a. Experimental investigation of short-crested wave breaking in a laboratory directional wave basin. Design Safe doi:https://doi.org/10.17603/ds2-qgd5-jk92.

Baker, C.M., Moulton, M., Palmsten, M.L., Brodie, K., Nuss, E., Chickadel, C.C., 2023b. Remotely sensed short-crested breaking waves in a laboratory directional wave basin. Coastal Engineering , 104327URL: https://www.sciencedirect.com/science/article/pii/S0378383923000510, doi:10.1016/j.coastaleng.2023.104327.

Blayo, E., Debreu, L., 2005. Revisiting open boundary conditions from the point of view of characteristic variables. Ocean Modelling 9, 231–252. URL: https://www.sciencedirect.com/science/article/pii/S1463500304000447, doi:10.1016/j.ocemod.2004.07.001.

Boehm, A.B., Keymer, D.P., Shellenbarger, G.G., 2005. An analytical model of enterococci inactivation, grazing, and transport in the surf zone of a marine beach. Water Research 39, 3565–3578. URL: https://linkinghub.elsevier.com/retrieve/pii/S0043135405003611, doi:10.1016/j.watres.2005.06.026.

Castelle, B., 2016. Rip current types, circulation and hazard. Earth-Science Reviews 163, 1–21. URL: https://www.sciencedirect.com/science/article/pii/S0012825216303117, doi:10.1016/j.earscirev.2016.09.008. publisher: Elsevier.

Clark, D.B., Elgar, S., Raubenheimer, B., 2012. Vorticity generation by short-crested wave breaking. Geophysical Research Letters 39. URL: https://onlinelibrary.

wiley.com/doi/abs/10.1029/2012GL054034, doi:10.1029/2012GL054034. _eprint: https://onlinelibrary.wiley.com/doi/pdf/10.1029/2012GL054034.

Dalrymple, R.A., 1975. A mechanism for rip current generation on an open coast. Journal of Geophysical Research (1896-1977) 80, 3485–3487. URL: https://onlinelibrary.wiley.com/doi/abs/10.1029/JC080i024p03485, doi:10.1029/JC080i024p03485. _eprint: https://onlinelibrary.wiley.com/doi/pdf/10.1029/JC080i024p03485.

Debreu, L., Marchesiello, P., Penven, P., Cambon, G., 2012. Two-way nesting in split-explicit ocean models: Algorithms, implementation and validation. Ocean Modelling 49-50, 1–21. URL: https://www.sciencedirect.com/science/article/pii/S1463500312000480, doi:10.1016/j.ocemod.2012.03.003.

Feddersen, F., Clark, D.B., Guza, R.T., 2011. Modeling surf zone tracer plumes: 1. Waves, mean currents, and low-frequency eddies. Journal of Geophysical Research: Oceans 116. URL: https://onlinelibrary.wiley.com/doi/abs/10.1029/2011JC007210, doi:10.1029/2011JC007210. _eprint: https://onlinelibrary.wiley.com/doi/pdf/10.1029/2011JC007210.

Fowler, R.E., Dalrymple, R.A., 1990. Wave Group Forced Nearshore Circulation. pp. 729–742.

Goda, Y., 2000. Random Seas and Design of Maritime Structures. volume 15 of *Advanced Series on Ocean Engineering*. 2 ed., WORLD SCIENTIFIC. URL: http://www.worldscientific.com/worldscibooks/10.1142/3587, doi:10.1142/3587.

Hally-Rosendahl, K., Feddersen, F., Guza, R.T., 2014. Cross-shore tracer exchange between the surfzone and inner-shelf. Journal of Geophysical Research: Oceans 119, 4367–4388. URL: https://onlinelibrary.wiley.com/doi/abs/10.1002/2013JC009722, doi:10.1002/2013JC009722. _eprint: https://onlinelibrary.wiley.com/doi/pdf/10.1002/2013JC009722.

Higuera, P., Losada, I.J., Lara, J.L., 2015. Three-dimensional numerical wave generation with moving boundaries. Coastal Engineering 101, 35–47. doi:10.1016/j.coastaleng.2015.04.003.

Jefferys, E.R., 1987. Directional seas should be ergodic. Applied Ocean Research 9, 186–191. URL: https://www.sciencedirect.com/science/article/pii/0141118787900010, doi:10.1016/0141-1187(87)90001-0.

Johnson, D., Pattiaratchi, C., 2004. Transient rip currents and nearshore circulation on a swell-dominated beach. Journal of Geophysical Research: Oceans 109. URL: https://onlinelibrary.wiley.com/doi/abs/10.1029/2003JC001798, doi:10.1029/2003JC001798. _eprint: https://onlinelibrary.wiley.com/doi/pdf/10.1029/2003JC001798.

Johnson, D., Pattiaratchi, C., 2006. Boussinesq modelling of transient rip currents. Coastal Engineering 53, 419–439. URL: https://www.sciencedirect.com/science/article/pii/S0378383905001730, doi:10.1016/j.coastaleng.2005.11.005.

Kumar, N., Feddersen, F., 2017. A new offshore transport mechanism for shoreline-released tracer induced by transient rip currents and stratification. Geophysical Research Letters 44, 2843–2851. URL: https://onlinelibrary.wiley.com/doi/abs/10.1002/2017GL072611, doi:10.1002/2017GL072611. _eprint: https://onlinelibrary.wiley.com/doi/pdf/10.1002/2017GL072611.

Longuet-Higgins, M.S., 1956. The refraction of sea waves in shallow water. Journal of Fluid Mechanics 1, 163–176. doi:10.1017/S0022112056000111.

Marchesiello, P., Auclair, F., Debreu, L., McWilliams, J., Almar, R., Benshila, R., Dumas, F., 2021. Tridimensional nonhydrostatic transient rip currents in a wave-resolving model. Ocean Modelling 163, 101816. URL: https://linkinghub.elsevier.com/retrieve/pii/S1463500321000676, doi:10.1016/j.ocemod.2021.101816.

Marchesiello, P., Benshila, R., Almar, R., Uchiyama, Y., McWilliams, J.C., Shchepetkin, A., 2015. On tridimensional rip current modeling. Ocean Modelling 96, 36–48. URL: https://www.sciencedirect.com/science/article/pii/S1463500315001122, doi:10.1016/j.ocemod.2015.07.003.

Marchesiello, P., Chauchat, J., Shafiei, H., Almar, R., Benshila, R., Dumas, F., Debreu, L., 2022. 3D wave-resolving simulation of sandbar migration. Ocean Modelling 180, 102127. URL: https://www.sciencedirect.com/science/article/pii/S146350032200141X, doi:10.1016/j.ocemod.2022.102127.

Marchesiello, P., McWilliams, J.C., Shchepetkin, A., 2001. Open boundary conditions for long-term integration of regional oceanic models. Ocean Modelling 3, 1–20. URL: https://www.sciencedirect.com/science/article/pii/S1463500300000135, doi:10.1016/S1463-5003(00)00013-5.

Marchesiello, P., Treillou, S., 2023. Correction of GLS turbulence closure for wave-resolving models with stratification. Ocean Modelling 184, 102212. URL: https://www.sciencedirect.com/science/article/pii/S1463500323000537, doi:10.1016/j.ocemod.2023.102212.

Miles, M.D., Funke, E.R., 1989. A Comparison of Methods for Synthesis of Directional Seas. Journal of Offshore Mechanics and Arctic Engineering 111, 43–48. URL: https://doi.org/10.1115/1.3257137, doi:10.1115/1.3257137.

Moulton, M., Suanda, S.H., Garwood, J.C., Kumar, N., Fewings, M.R., Pringle, J.M., 2023. Exchange of Plankton, Pollutants, and Particles Across the Nearshore Region. Annual Review of Marine Science 15, 167–202. URL: https://doi.org/10.1146/annurev-marine-032122-115057, doi:10.1146/annurev-marine-032122-115057. _eprint: https://doi.org/10.1146/annurev-marine-032122-115057.

Nuss, E.S., Moulton, M., Suanda, S., Baker, C.M., in review. Modeled surf-zone eddies on a laboratory scale barred beach with varying wave conditions.

Pascal, R., 2012. Quantification of the influence of directional sea state parameters over the performances of wave energy converters. Ph.D. thesis.

Pascal, R., Bryden, I., 2011. Directional spectrum methods for deterministic waves. Ocean Engineering 38, 1382–1396. URL: https://www.sciencedirect.com/science/article/pii/S0029801811001119, doi:10.1016/j.oceaneng.2011.05.021.

Peregrine, D., 1998. Surf Zone Currents. Theoretical and Computational Fluid Dynamics 10, 295–309. URL: https://doi.org/10.1007/s001620050065, doi:10.1007/s001620050065.

Salatin, R., Chen, Q., Bak, A.S., Shi, F., Brandt, S.R., 2021. Effects of Wave Coherence on Longshore Variability of Nearshore Wave Processes. Journal of Geophysical Research: Oceans 126, e2021JC017641. URL: https://onlinelibrary.wiley.com/doi/abs/10.1029/2021JC017641, doi:10.1029/2021JC017641. _eprint: https://onlinelibrary.wiley.com/doi/pdf/10.1029/2021JC017641.

Shanks, A.L., Morgan, S.G., MacMahan, J., Reniers, A.J.H.M., 2017. Alongshore variation in barnacle populations is determined by surf zone hydrodynamics. Ecological Monographs 87, 508–532. URL: https://onlinelibrary.wiley.com/doi/abs/10.1002/ecm.1265, doi:10.1002/ecm.1265. _eprint: https://onlinelibrary.wiley.com/doi/pdf/10.1002/ecm.1265.

Shchepetkin, A.F., McWilliams, J.C., 2005. The regional oceanic modeling system (ROMS): a split-explicit, free-surface, topography-following-coordinate oceanic model. Ocean Modelling 9, 347–404. URL: https://www.sciencedirect.com/science/article/pii/S1463500304000484, doi:10.1016/j.ocemod.2004.08.002.

Smit, P.B., Janssen, T.T., 2013. The evolution of inhomogeneous wave statistics through a variable medium. Journal of Physical Oceanography 43, 1741 – 1758.

Spydell, M.S., Feddersen, F., Suanda, S., 2019. Inhomogeneous Turbulent Dispersion across the Nearshore Induced by Surfzone Eddies 49, 1015–1034. URL: https://www.proquest.com/docview/2398117576/abstract/8FDFDB45F6BA4BEBPQ/1, doi:10.1175/JPO-D-18-0102.1. num Pages: 1015-1034 Place: Boston, United States Publisher: American Meteorological Society.

Suanda, S.H., Feddersen, F., 2015. A self-similar scaling for cross-shelf exchange driven by transient rip currents: SCALING TRANSIENT RIP CURRENT EXCHANGE. Geophysical Research Letters 42, 5427–5434. URL: http://doi.wiley.com/10.1002/2015GL063944, doi:10.1002/2015GL063944.

Tang, E.C.S., Dalrymple, R.A., 1989. Rip Currents and Wave Groups, in: Seymour, R.J. (Ed.), Nearshore Sediment Transport. Springer US, Boston, MA, pp. 205–230. URL: https://doi.org/10.1007/978-1-4899-2531-2_22, doi:10.1007/978-1-4899-2531-2_22.

Warner, J.C., Defne, Z., Haas, K., Arango, H.G., 2013. A wetting and drying scheme for ROMS. Computers & Geosciences 58, 54–61. URL: https://www.sciencedirect.com/science/article/pii/S0098300413001362, doi:10.1016/j.cageo.2013.05.004.

Wei, G., Kirby, J.T., Sinha, A., 1999. Generation of waves in Boussinesq models using a source function method. Coastal Engineering 36, 271–299. URL: https://www.sciencedirect.com/science/article/

pii/S0378383999000095, doi:10.1016/S0378-3839(99)00009-5.

Woodward, E., Beaumont, E., Russell, P., Wooler, A., Macleod, R., 2013. Analysis of Rip Current Incidents and Victim Demographics in the UK. Journal of Coastal Research , 850–855URL: https://www.jstor.org/stable/26482078. publisher: Coastal Education & Research Foundation, Inc.

Wu, X., Feddersen, F., Giddings, S.N., 2021. Diagnosing Surfzone Impacts on Inner-Shelf Flow Spatial Variability Using Realistic Model Experiments with and without Surface Gravity Waves. Journal of Physical Oceanography 51, 2505–2515. URL: https://journals.ametsoc.org/view/journals/phoc/51/8/JPO-D-20-0324.1.xml, doi:10.1175/JPO-D-20-0324.1. publisher: American Meteorological Society Section: Journal of Physical Oceanography.

Zhang, Y., Shi, F., Kirby, J.T., Feng, X., 2022. Phase-Resolved Modeling of Wave Interference and Its Effects on Nearshore Circulation in a Large Ebb Shoal-Beach System. Journal of Geophysical Research: Oceans 127, e2022JC018623. URL: https://onlinelibrary.wiley.com/doi/abs/10.1029/2022JC018623, doi:10.1029/2022JC018623. _eprint: https://onlinelibrary.wiley.com/doi/pdf/10.1029/2022JC018623.

Zijlema, M., Stelling, G., Smit, P., 2011. SWASH: An operational public domain code for simulating wave fields and rapidly varied flows in coastal waters. Coastal Engineering 58, 992–1012. URL: https://www.sciencedirect.com/science/article/pii/S0378383911000974, doi:10.1016/j.coastaleng.2011.05.015.

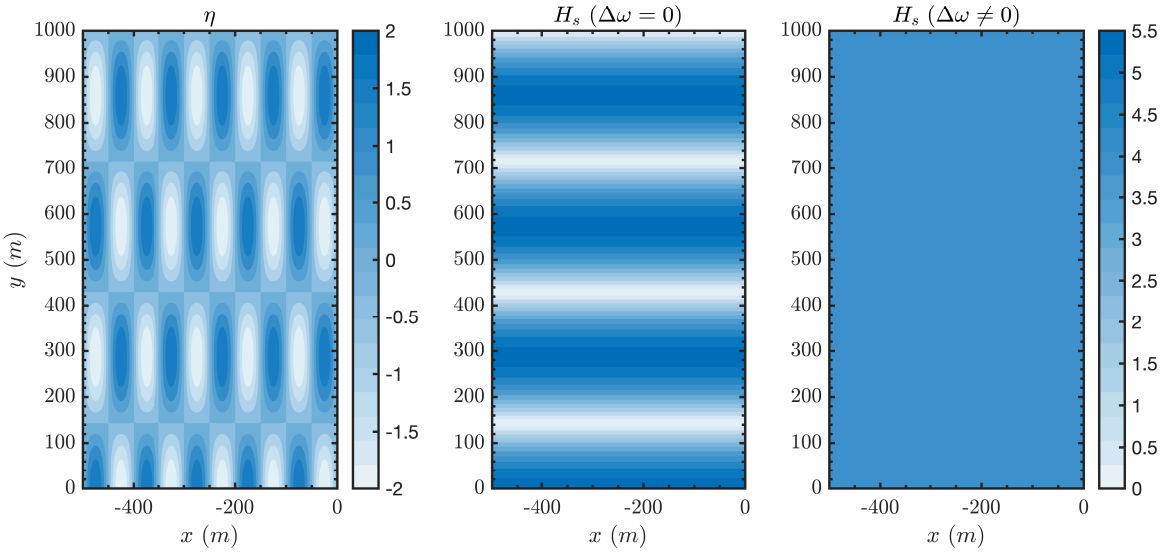

Figure 1: Illustration of the coherent interference of two deep water wave trains propagating to the right at an angle of ± 10 degrees to the x axis (amplitude 1 m, wavelength 100 m, period 10 s). The left panel shows a snapshot of surface elevation η featuring short-crested waves $\sim$286 m long, migrating along the y axis with a speed varying with the frequency difference $\Delta\omega$ between wave trains; the central panel shows H_s for $\Delta\omega = 0$, i.e. with no longshore migration. The right-hand panel shows the significant wave height H_s in the case where $\Delta\omega \neq 0$. In the first case, coherent interference produces a persistent H_s pattern that should create stationary rip currents as they break on the beach. In the second case, no pattern is produced and no persistent rip currents are expected.

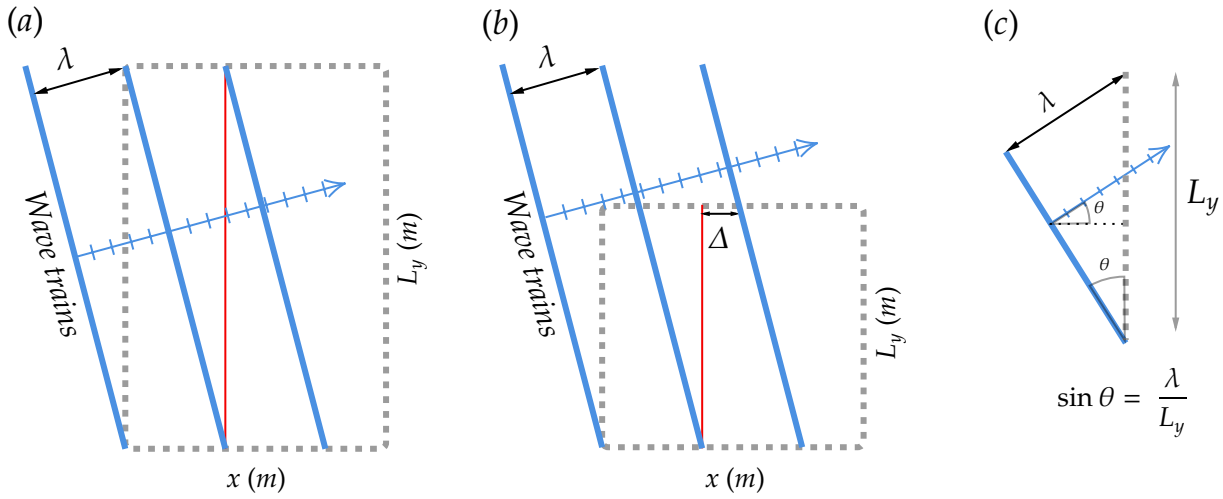

Figure 2: Schematic view of the periodicity condition for obliquely incident long-crested waves over a finite domain. (a) the periodicity is respected by the right combination of domain length L_y and wavelength λ; (b) the domain size breaks periodicity by introducing a small gap Δ between wave crests at the northern and southern boundaries; (c) relationship linking wave direction to L_y and λ to ensure periodicity. Note that the scheme assumes only one periodic wavelength for simplicity but there can be an integer number p of smaller wavelength (the relation is then $\sin\theta = \frac{p\lambda}{L_y}$).

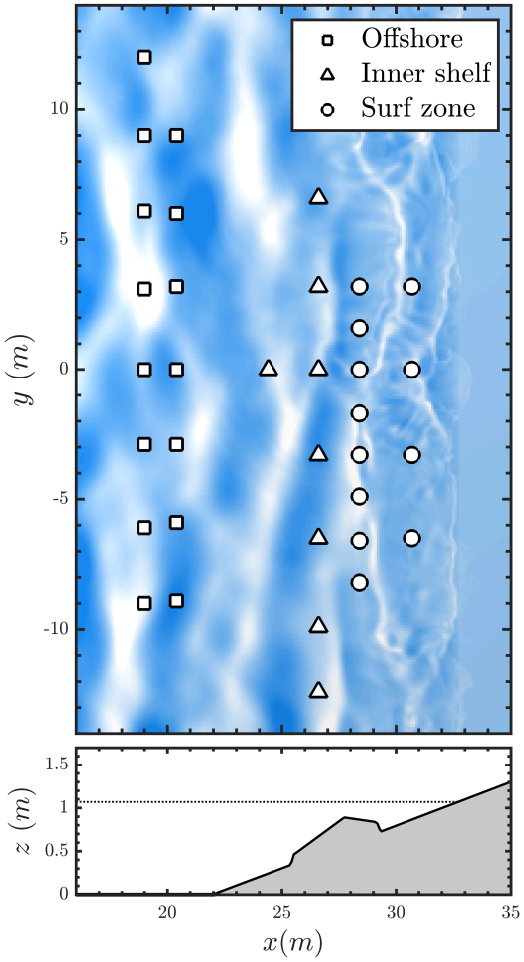

Figure 3: (Top) Snapshot of simulated free surface elevation in the case G1d ($\sigma_\theta = 26.1°$) after 15 minutes. The stations where experimental data were collected are displayed. Squares represent offshore wire resistance gauges, triangles innershelf pressure gauges and circles surf zone pressure gauges. (Bottom) Cross-shore profile of the bathymetry (shaded) and still water level (dashed line, at 1.07 m).

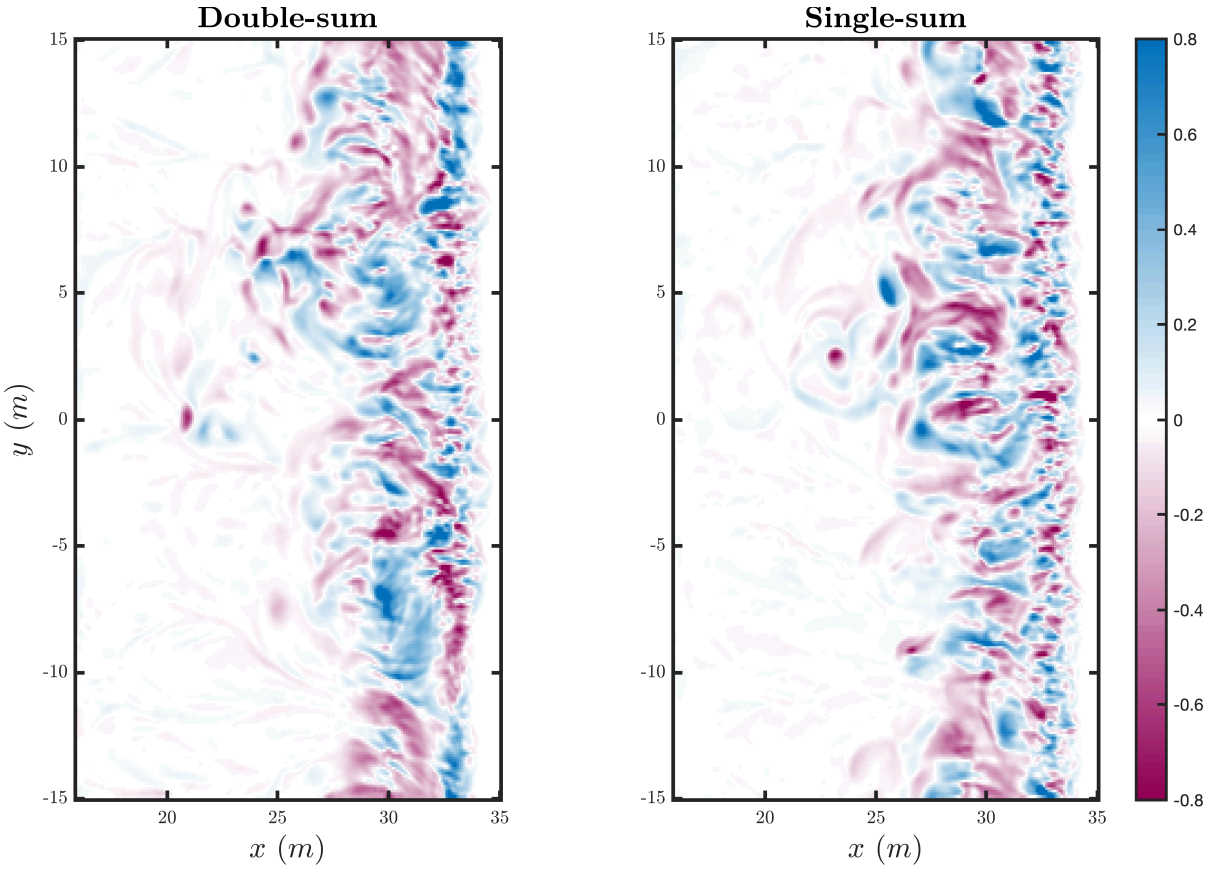

Figure 4: Snapshot of instantaneous surface vertical vorticity ω_z (s^{-1}) for the double-sum (left, 50 freq.) and single-sum (right) wavemakers in the G1d experiment ($\sigma_\theta = 26.1°$).

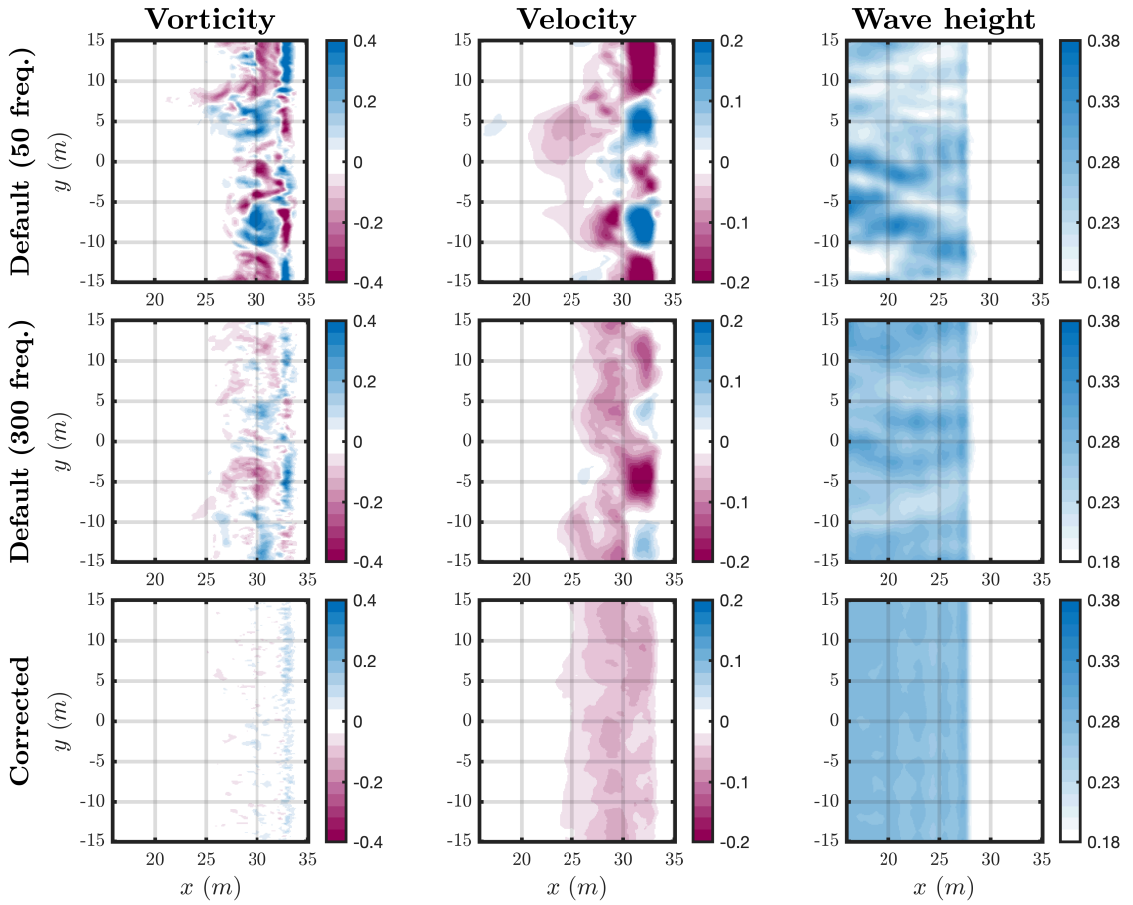

Figure 5: Time-averaged ($t = 10 - 30$ min) surface vertical vorticity ω_z (s^{-1}, left), alongshore velocity v ($\mathrm{m.s}^{-1}$, middle) and significant wave height H_s (m, right) for the double-sum (top: $N = 50$ freq., middle: $N = 300$ freq.) and single-sum (bottom: $N = 50$ freq.) wavemakers in the G1d case ($\sigma_\theta = 26.1°$).

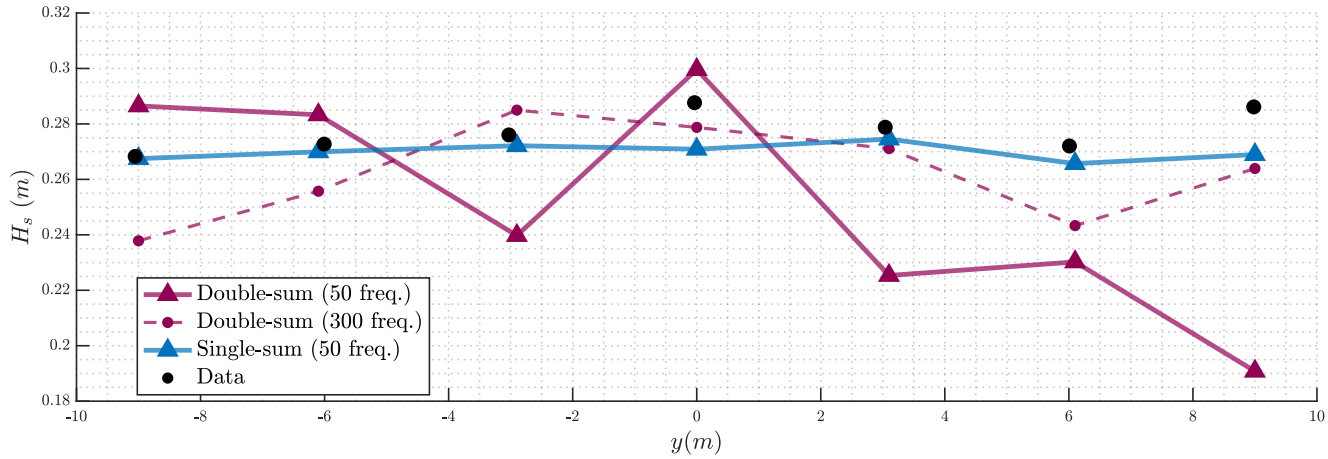

Figure 6: Significant wave height H_s (m) for G1d ($\sigma_\theta = 26.1°$) at all offshore stations along the coast ($x = 19.0$m, $-9 < y < 9$m). The data (black circles) is from wave gauges and the model values from the double-sum (pink triangles for $N = 50$ freq. and pink dots for $N = 300$ freq.) and single-sum (blue triangles) wavemaker simulations computed at the same locations.

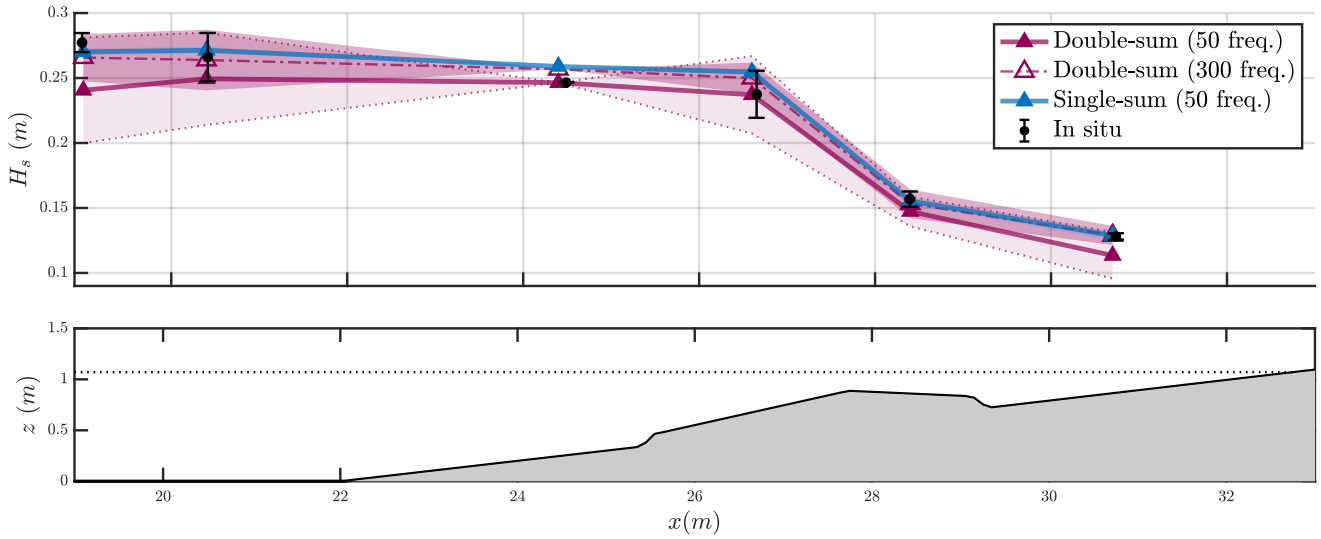

Figure 7: (Top) Cross-shore profile of longshore and time-averaged significant wave height H_s (m) for G1d ($\sigma_\theta = 26.1°$). Comparison is made between experimental in-situ data (black dots) and the double-sum (pink solid line for $N = 50$ freq. and pink dashed line for $N = 300$ freq.) and single-sum (blue triangles) wavemaker simulations. The longshore standard deviation is shown as shaded areas for the model solutions, and as an error bar for the in-situ data. The longshore standard deviation for the double-sum (50 freq.) wavemaker simulation is enhanced with dashed fine pink line for readibility. (Bottom) Cross-shore bathymetry profile (shaded) and still water level (dashed line, at 1.07 meters).

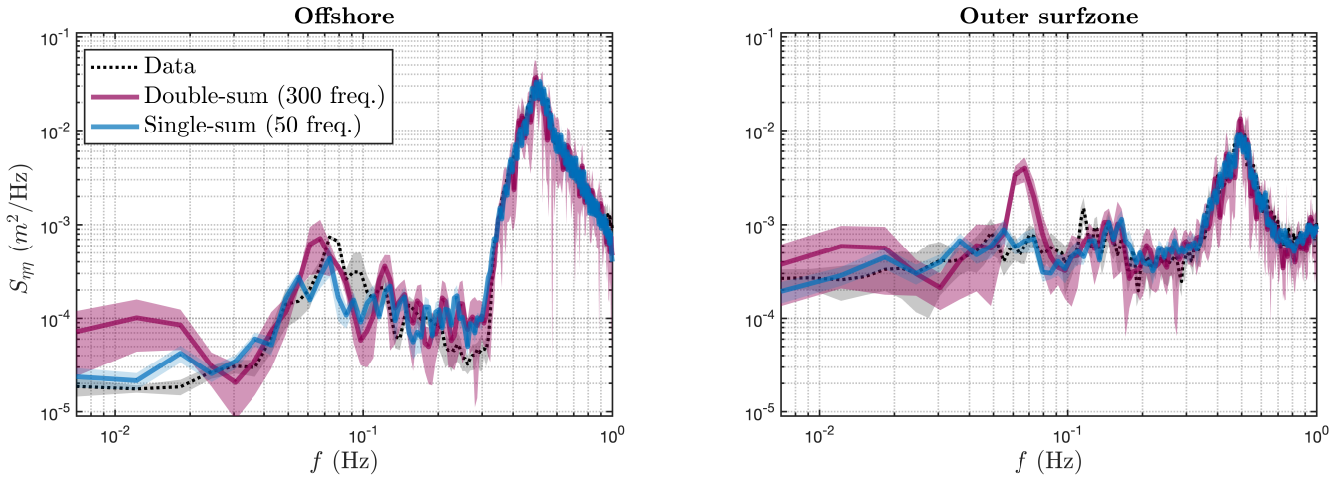

Figure 8: Longshore-averaged power spectra of free surface ($S_{\eta\eta}$) as a function of frequency (f) for stations located offshore (left, $x = 19.0$m, $-9 < y < 9$m) and in the outer surfzone (right, $x = 28.4$m, $-8 < y < 3$m). Spectra from experimental data are shown as black dots, while those from simulations with the double-sum (300 freq.) and single-sum wavemakers are shown as pink and blue lines, respectively. The longshore standard deviations of the model and data spectra are represented by shaded areas.

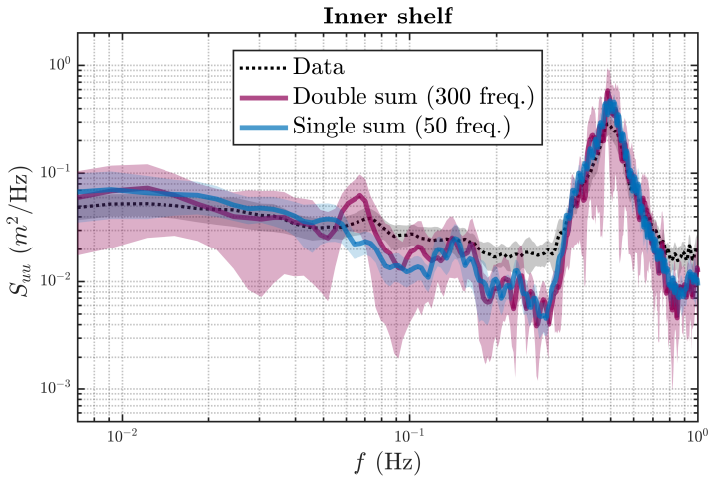

Figure 9: Longshore-average power spectra of the cross-shore velocity (S_{uu}) as a function of frequency (f) for station located in the innershelf (left, $x = 26.6$m, $-10 < y < 10$m). The spectrum from experimental data is shown as black dots, while those from simulations with the double-sum (300 freq.) and single-sum wavemakers are shown as pink and blue lines, respectively. The longshore standard deviations of the model and data spectra are represented by shaded areas.